FULL PAPER

Open Access

Characterized source model of the 2013 Lushan earthquake (M_w 6.6) by the empirical Green's function method

Hao Wu[1]* , Kojiro Irikura[2], Ken Miyakoshi[3] and Kazuhiro Somei[3]

Abstract

Ground motions near the source area of the mainshock of the 2013 Lushan earthquake (M_w 6.6) in Sichuan Province in China were reproduced using the characterized source model and the empirical Green's function method (EGFM). The best-fit characterized source model consisted of one strong motion generation area (SMGA) and a background area. The synthesized ground motions of the characterized source model were in fairly good agreement with the observed ground motions in the frequency range from 0.5 to 30.0 Hz at ten strong motion stations. For the 2013 Lushan earthquake (M_w 6.6), both the relationships between the SMGA and the seismic moment, and those between the flat amplitude of the acceleration source spectrum in the short period and the seismic moment almost followed the empirical scaling relationships of inner fault parameters developed for crustal earthquakes. The reasons for the largest peak ground acceleration (PGA) (> 1 g) in the strong-motion observation history of China recorded at the 51BXD strong motion station were investigated from the source and site effects. We found that the directivity effect did not contribute to the largest record by comparing the effect of different positions of the rupture starting point on the synthesized ground motions. The nonlinear effect of shallow layers was negligible, as indicated by the similarity of the earthquake H/V spectral ratios between the mainshock and EGF events. A large shear-wave velocity contrast might not exist in the shallow layers as the station was situated on the slope of a small rock hill. Finally, we agreed with previous studies that the hanging-wall effect and topographic effect might be the reasons for generating the largest record at Station 51BXD.

Keywords: Strong motion generation area, Empirical Green's function method, The 2013 Lushan earthquake (M_w 6.6), Empirical scaling relationships of inner fault parameters

*Correspondence: wh_ce@sdjzu.edu.cn
[1] School of Civil Engineering, Shandong Jianzhu University, Fengming Road 1000, Jinan, Shandong 250101, China
Full list of author information is available at the end of the article

Wu *et al. Earth, Planets and Space*   (2022) 74:50
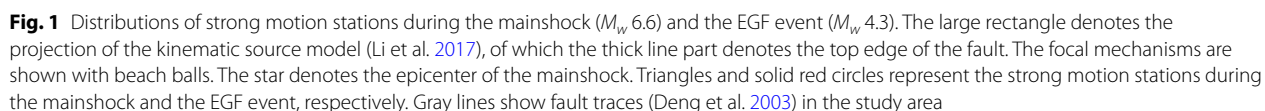
Page 2 of 15

Graphical Abstract
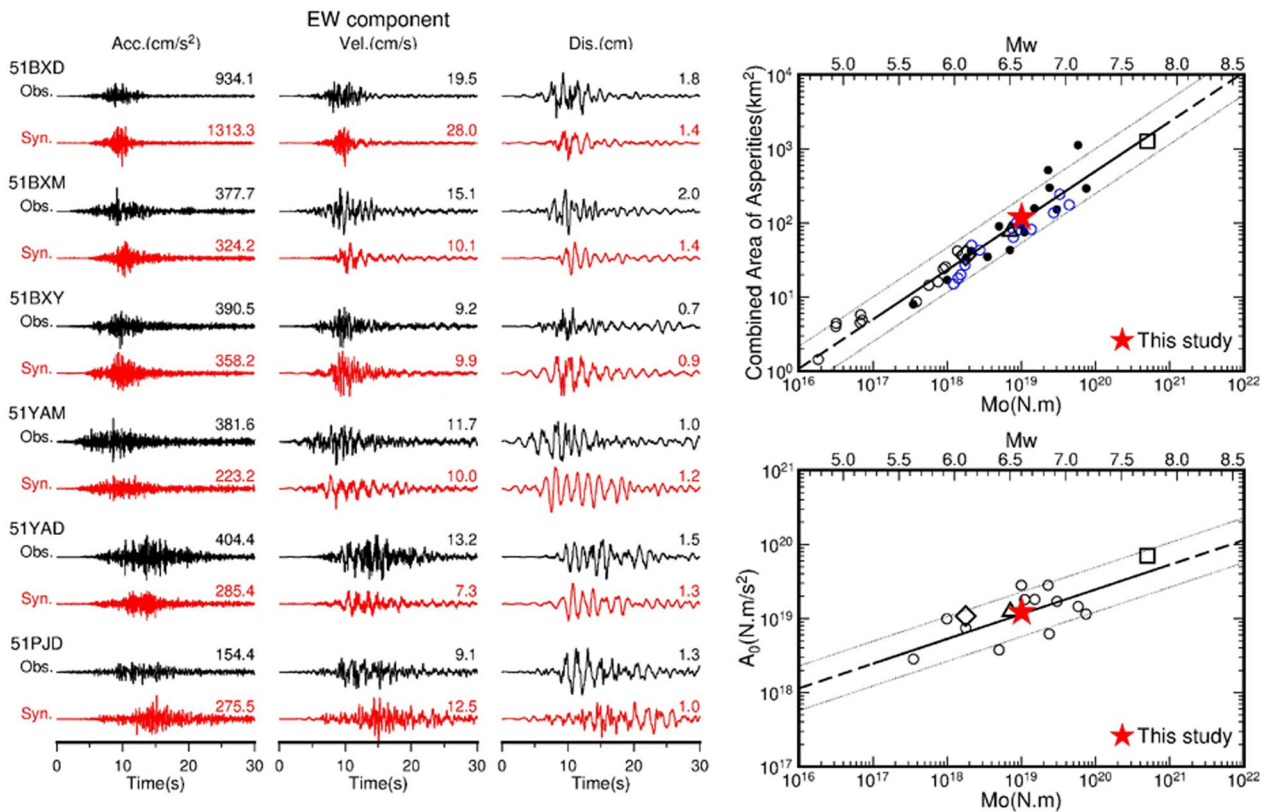
Introduction

The 2013 Lushan earthquake (M_w 6.6) struck Lushan County, Ya'an City, Sichuan Province, China at 08:02 on April 20, 2013 (Beijing time, 00:02 on April 20, 2013, UTC). The mainshock caused considerable damage to buildings; 196 people died and 21 people were reported missing. The strong ground motions during the mainshock of the 2013 Lushan earthquake were recorded by as many as 114 strong-motion stations including some near-fault stations, as shown in Fig. 1. The largest PGA was 1005 cm/s² calculated from the uncorrected (raw) acceleration record in the east–west (EW) component at Station 51BXD approximately 16 km from the epicenter, which was the first time that 1 g was exceeded in the strong motion observation history of China. It is important to clarify the source and site effects to interpret this large value.

To date, the source rupture process of this earthquake has been illuminated by many kinematic source models developed with the waveform inversion method using teleseismic data (Liu et al. 2013), joint inversion of strong-motion data and teleseismic data (Hao et al. 2013; Zhang et al. 2014), and joint inversion of strong-motion data, teleseismic data and GPS records (Li et al. 2017). Despite the different data sets and methods, these kinematic source models have much in common in that the mainshock ruptured a blind thrust fault in the southern part of the Longmen Shan fault belt and that large slip areas surrounded the hypocenter. The synthesized ground motions using these inverted source models agreed well with the long-period (e.g., > 1 s) observed ground motions, whereas they could not match the observed ground motions at near-source stations in the period range of engineering interests (e.g., 0.1–10.0 s). Then, the characterized source model consisting of several asperities and a background area in the seismogenic zone was applied to synthesize the ground motions. This model involves outer and inner fault parameters. The outer fault parameters are defined to outline the overall picture of the target earthquake, such as the entire source area and seismic moment, while the inner fault parameters are defined by asperities with large slips and stress

Fig. 1 Distributions of strong motion stations during the mainshock (M_w 6.6) and the EGF event (M_w 4.3). The large rectangle denotes the projection of the kinematic source model (Li et al. 2017), of which the thick line part denotes the top edge of the fault. The focal mechanisms are shown with beach balls. The star denotes the epicenter of the mainshock. Triangles and solid red circles represent the strong motion stations during the mainshock and the EGF event, respectively. Gray lines show fault traces (Deng et al. 2003) in the study area

drops. Strong ground motions of engineering interest are mostly generated from asperities. Therefore, the asperities are called strong motion generation areas (SMGAs).

The outer and inner fault parameters follow specific scaling relationships for crustal earthquakes (Somerville et al. 1999; Dan et al. 2001; Irikura and Miyake 2001,

Wu *et al. Earth, Planets and Space*   (2022) 74:50

Page 4 of 15

2011; Miyake et al. 2003; Miyakoshi et al. 2020). However, the empirical scaling relationships of inner fault parameters for crustal earthquakes in China have not been adequately investigated.

In this study, we elaborate the process to construct the characterized source model of the mainshock with the empirical Green's function method (EGFM) (Irikura 1986) and then examine whether the inner fault parameters of the mainshock agree with the empirical scaling relationships thus far developed. Finally, we quantitatively discuss the source and site effects on the largest record (PGA > 1 g) at Station 51BXD.

Methodology

The empirical Green's function method (EGFM) was first proposed by Hartzell (1978) and then revised by Kanamori (1979) and Irikura (1983, 1986). The ground motions of a large event are expressed as a superposition of the ground motions of a small event in Eqs. (1)–(3) (Irikura 1986):

$$U(t) = \sum_{i=1}^{N} \sum_{j=1}^{N} \frac{r}{r_{ij}} F(t - t_{ij}) * (C \cdot u(t)). \qquad (1)$$

$$t_{ij} = \frac{r_{ij} - r_o}{V_s} + \frac{\xi_{ij}}{V_r}, \qquad (2)$$

$$F(t) = \delta(t) + \frac{1}{n'(1 - 1/e)} \cdot \sum_{K=1}^{(N-1)n'} \left[\exp\left\{ \frac{-(k-1)}{(N-1)n'} \right\} \delta\left\{ t - \frac{(k-1)}{(N-1)n'} \right\} \right]. \qquad (3)$$

Where $U(t)$ represents the ground motions of a large event, and $u(t)$ is the ground motions of a small event regarded as the empirical Green's functions (EGFs). The subscripts i and j are indices increasing along the strike and dip directions, respectively. The terms r, r_{ij}, and r_0 are the respective distances from the station to the hypocenter of the small event, from the station to the (i,j) subfault, and from the station to the rupture starting point on the fault plane of the large event. In addition, ξ_{ij} is the distance between the rupture starting point and the (i,j) subfault. V_s and V_r are the S-wave velocities in the source region and rupture velocity on the fault plane, respectively. $F(t)$ is the correction function of slip velocity between large and small events which was modified by Irikura et al. (1997). The parameters, N and C, are the ratios of fault sizes (length and width) and stress drops between the large and small events, respectively. Furthermore, n' is the division number to shift the artificial periodicity to a frequency higher than that of interests, e Euler's number, and Γ the rise time of the large event.

The formulation of the EGFM in Eq. (1) implies that the synthesized ground motions consider the contribution of the Green's functions from the far-field term only. Because the empirical Green's functions contain the contributions of near-, intermediate- and far-field terms, the synthesized ground motions naturally contain the contributions from all terms. According to Nozu (2006), the Fourier spectral ratio of total waves corresponding to the near-, intermediate- and far-field terms to the far-field S-wave term approaches 1 when the normalized frequency ($= 2\pi f r / V_s$, r is the hypocentral distance) is larger than 8. This means that the contributions of the near- and intermediate-field terms can be neglected only if $f > 8 V_s / 2\pi r$. As V_s in the source region is 3.50 km/s (Han et al. 2014), and the shortest hypocentral distance is approximately 20 km, the far-field S-wave term in the synthesized ground motions is comparable with that of the total terms without any corrections at frequencies larger than 0.2 Hz.

We adopted the method proposed by Miyake et al. (1999) to estimate the fault size of the EGF event, N and C by fitting the theoretical source spectral ratio to the observed one. The observed source spectral ratio is estimated from the ratio of the observed Fourier spectrum (vector summation of two horizontal components) removing the path effect between large and small events, while the theoretical source spectral ratio is expressed as the following equation:

$$SSRF(f) = \frac{M_o}{m_o} \frac{1 + (f/f_{ca})^2}{1 + (f/f_{cm})^2}, \qquad (4)$$

where M_o and m_o are the seismic moments of large and small events, respectively, and f_{ca} and f_{cm} are the corner frequencies of large and small events, respectively.

Once the best-fit theoretical source spectral ratio is determined by searching the minimum of weighted least squares (Miyake et al. 2003), the corner frequencies f_{ca} and f_{cm} are directly obtained according to Eq. (4). The proportional parameters, N and C, are estimated from Eq. (5). The fault size r_a and stress drop $\Delta\sigma_a$ of the EGF event are estimated by applying Eq. (6) (Eshelby 1957; Brune 1970, 1971):

$$N = \frac{f_{ca}}{f_{cm}}, \quad C = \left(\frac{M_o}{m_o}\right)\left(\frac{f_{cm}}{f_{ca}}\right)^3. \qquad (5)$$

$$r_a = \frac{2.34 V_s}{2\pi f_{ca}}, \ \Delta\sigma_a = \frac{7}{16}\frac{m_o}{r_a^3}. \tag{6}$$

Except for the above parameters (i.e., N, C, r_a), we determine the position indices (i, j) of the rupture starting point within the SMGAs, V_r and Γ, by applying the adaptive simulated annealing (ASA) algorithm, which employs a more efficient sampling of the parameter space than the conventional simulated annealing algorithm. We gave a brief introduction to the ASA algorithm by referring to Satoh (2006).

Let $\mathbf{x}(t)$ be the vector composed of parameters $x_i(t)$ (i.e., C, N, i, j, V_r and Γ). Here, $x_i(t)$ is generated from the generating function by use of random variable Δx_i as expressed in Eq. (7). Δx_i is generated from the generating temperature $T_{i,gen}$ and uniform random value u as expressed in Eq. (8):

$$x_i(t) = x_i(t-1) + (B_i - A_i)\Delta x_i, \ x_i \in [A_i, B_i]. \tag{7}$$

$$\Delta x_i = \text{sgn}\left(u_i - \frac{1}{2}\right) T_{i,gen} \cdot \left[\left(1 + 1/T_{i,gen}\right)^{2u_{i-1}} - 1\right], \ \Delta x_i \in [-1, 1], \tag{8}$$

where $T_{i,gen}$ is calculated from the temperature reduction function as

$$T_{i,gen}(k_i) = T_{i,gen}(0) \exp\left(-c_i k_i^\alpha\right), \tag{9}$$

where k is an annealing factor for each generating temperature, c is a constant defining the relative width of the generating distributions, and α is a factor associated with the speed of temperature decrease. The values of the parameters-$T_{i,gen}(0)$, c, and α are set to 1.0, 1, and 0.6, respectively, based on several numerical experiments.

Once new values for $\mathbf{x}(t)$ are generated, the difference of the misfit functions between new and previous is computed as

$$\Delta E = E(x(t)) - E(x(t-1)), \tag{10}$$

where $E(\mathbf{x})$ is the misfit function defined by the residual between synthesized and observed records for acceleration envelopes and displacement waveforms (Miyake et al. 1999).

The new values $\mathbf{x}(t)$ are accepted if $\Delta E < 0$. If $\Delta E > 0$, $\mathbf{x}(t)$ is accepted if the uniform random value u is less than P, which is expressed as the following equation:

$$P = \exp\left(-\frac{\Delta E}{T(k)}\right), \tag{11}$$

where the acceptance temperature is calculated as Eq. (9).

Determination of parameters required for the EGFM

The characterized source model in this study is composed of a SMGA consisting of $N \times N$ subfaults along the strike and dip directions, and a background area in the seismogenic zone on the fault plane. Because the background area mostly contributes to long-period strong ground motions (Kurahashi and Irikura 2010), we estimated the strong ground motions only from the contribution of the SMGA neglecting the contributions from the background area. The number of SMGAs generally depends on the complexity of the source rupture process. For large magnitude earthquakes, multiple SMGAs seem to be distributed randomly (e. g. Kamae and Irikura 1998; Kurahashi and Irikura 2010, 2013). For the 2013 Lushan earthquake, several source–rupture–process studies based on waveform inversion analyses were common in that the large slip area was concentrated around the hypocenter. Therefore, it is reasonable to suppose that one SMGA located in the large slip area of the kinematic source models is suitable for synthesizing the ground motions.

First, we selected an aftershock with M_w 4.3 as an EGF. The aftershock occurred near the SMGA on 22:16, April 21, 2013 (Beijing time, 14:16, April 21, 2013, UTC) and had a similar source mechanism (Yi et al. 2016) as the mainshock. The positions of hypocenters and source mechanisms for the mainshock and this aftershock are listed in Table 1. The difference in the dip and rake angles between the mainshock and the aftershock are influential on the radiation pattern of ground motions from the source over a longer period range but less influential on those over a shorter period range, as the radiation characteristics over a shorter period are naturally smoothed due to diffraction and scattering along propagation paths (Kamae and Irikura 1992). Moreover, the site effects are more influential on the mainshock ground motions in

Table 1 Information on the mainshock (Li et al. 2017) and the EGF event

Origin time (Beijing time)	2013/04/20, 08:02	2013/04/21, 22:16
Latitude, Longitude (º)	30.284, 102.956	30.339, 102.925[a]
Depth (km)	15	17.126[a]
M_w	6.6	4.32[b]
M_0 (N·m)	1.01×10^{19}	3.80×10^{15}[b]
Strike/dip/rake (º)	214.0/38.0/103.0	235.0/61.0/106.0[b]

[a] refers to Han et al. (2014)

[b] refers to Yi et al. (2016)

a shorter period of engineering interest. Therefore, it is acceptable even if the dip and rake angles of the aftershock are not identical to those of the mainshock. Figure 1 shows the distribution of strong motion stations and beach ball diagrams of source mechanisms for the mainshock and the EGF event. Figure 1 also shows the projection of the kinematic source model with a large rectangle. The kinematic source model developed by the waveform inversion method (Li et al. 2017) is adopted for constructing the characterized source model, as the hypocenter is close to the position determined by high-resolution relocation (Han et al. 2014). The ground motions of the M_w 4.3 aftershock at the stations, where the records of both the mainshock and the EGF event were available are regarded as EGFs. We synthesized ground motions at seven strong motion stations (e.g., 51BXD, 51BXM, 51BXY, 51YAM, 51QLY, 51YAD, 51PJD) surrounding the source region by applying the EGFM. The 51BXZ near-source station is excluded, as a strong nonlinear effect is observed (see details in the "Discussion" section).

Second, we estimated the inner fault parameters related to the SMGA from the source spectral ratios of the mainshock ground motions to the EGF ones. We employed the S-wave portion with a length of 40.96 s of the mainshock and EGF event to calculate the observed Fourier spectra. We followed the method of Miyake et al. (1999) to adopt the hypocenter distance for the mainshock and EGF events to remove the path effect ($Q_s(f) = 155f^{0.6804}$, Tao et al. 2016) from the Fourier spectra to obtain the observed source spectra. The average source spectral ratios and standard deviations for the target stations are shown with thick gray and dashed curves in Fig. 2. Three parameters, i.e., seismic moment ratio (M_o/m_o) between the mainshock and the EGF event, corner frequencies of the mainshock (f_{cm}) and the EGF event (f_{ca}), are required to estimate the theoretical source spectral ratio as expressed in Eq. (4). The ratio M_o/m_o is known from the moment magnitudes of the mainshock and the EGF event, while f_{cm} and f_{ca} are determined when the theoretical spectral ratio best fits the observed source spectral ratio in a specific frequency range. We set the lower frequency limit for fitting the observed source spectral ratio to be 0.5 Hz considering the low signal-to-noise ratio of observed ground motions and the upper frequency limit to be 30.0 Hz, which is below the cutoff frequency of the anti-aliasing filter of the seismograph. We determined the best fitting of the theoretical source spectral ratio (red curves in Fig. 2) to the average observed spectral ratio (thick curves in Fig. 2) in the frequency range of 0.5 to 30.0 Hz when $f_{ca} = 1.90$ Hz and $f_{cm} = 0.17$ Hz. Subsequently, we applied Eqs. (5) and (6) to calculate $N = 11$, $C = 2.12$, $r_a = 0.68$ km, and $\Delta\sigma_a = 4.85$ MPa. For small or
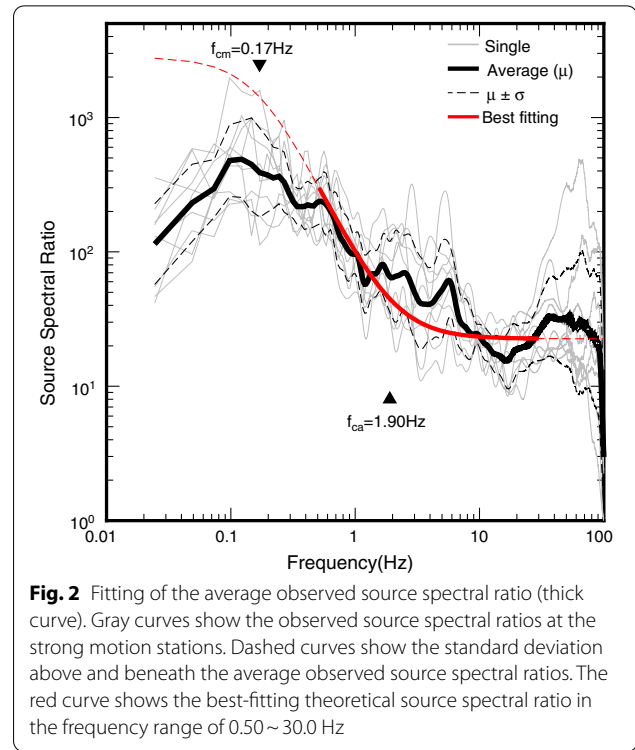

Fig. 2 Fitting of the average observed source spectral ratio (thick curve). Gray curves show the observed source spectral ratios at the strong motion stations. Dashed curves show the standard deviation above and beneath the average observed source spectral ratios. The red curve shows the best-fitting theoretical source spectral ratio in the frequency range of 0.50 ~ 30.0 Hz

moderate earthquakes, the fault length can be identical to the fault width; thus, the fault length or width of the EGF event is $\sqrt{\pi}r_a = 1.21$ km. It should be noted that the ground motions from the SMGA are approximately expressed as omega-squared spectra with a corner frequency f_{cSMGA} (Boatwright 1988; Miyake et al. 2003). Then, f_{cm} and M_o in Eq. (5) can be expressed with f_{cSMGA} and M_{oSMGA} (seismic moment of the SMGA), respectively (Miyake et al. 2003; Somei et al. 2020). Therefore, N and C can be regarded as the ratio of the fault size between the SMGA and the EGF event, and the ratio of the stress drop between the SMGA and the EGF event, respectively.

Third, we applied the ASA algorithm to determine the optimal values of the parameters required by the EGFM, such as i, j, V_r, Γ as well as N and C determined by fitting the observed source spectral ratio which are not sufficiently accuracy considering the small signal-to-noise ratio of the observed ground motions in the low frequency range. We fixed the rupture starting point at the hypocenter (Li et al. 2017) and kept the size of the fault length/width of the EGF event constant. Under the same acceptance temperature, the iteration of the ASA algorithm was carried out 5 times, and the search of indices (i, j) of the rupture starting point was carried out 10 times for each iteration, whereas the final value of k was set to 100. Therefore, the optimal parameters were determined when the misfit function reached the global minimum among the 5000 iterations. Table 2 lists the search

Wu *et al. Earth, Planets and Space*   *(2022) 74:50*

Page 7 of 15

Table 2 Parameters related to synthesizing ground motions by the EGFM

Parameters	Search ranges	Determined values
Rupture velocity (km/s)	$(0.55–0.95)*V_s$[a]	2.68
Rise time (s) for the EGF event	0.01–0.20	0.07[b]
C	1.28–3.87	2.68
N	7–12	9
Indices of rupture starting point	$(1–N, 1–N)$	(5, 4)

[a] $Vs = 3.5$ km/s

[b] Rise time for the mainshock $\Gamma = N\tau_a = 0.63$ s

range for each parameter in the second column. The search ranges for V_r and rise time-τ_a of the EGF event ($\Gamma = N\tau_a$ for the mainshock) are approximately assigned, while the upper and lower limits for C and N are evaluated by the fitting of the theoretical source spectral ratio to the observed ones as shown in dashed curves lying one standard deviation above and below the average observed source spectral ratio. In accordance with the fitting frequency range of the observed source spectral ratio, we applied a bandpass filter of 0.5–30.0 Hz beforehand to the waveforms with a time window of 30 s, which contains the S-wave portions at the seven target stations. Because step-like pulses were observed on the baseline of the records in the EW component at Station 51QLY for both the EGF event and the mainshock, we abandoned synthesizing the ground motions in the EW component to eliminate the special process of baseline correction.

Synthesized ground motions using the characterized source model

We obtained the best-fit SMGA of the characterized source model when the residuals between synthesized and observed records for the misfit function consisting of acceleration envelopes and displacement waveforms (Miyake et al. 1999) reached the global minimum throughout all iterations. The optimal values of the parameters, such as C, N, i, j, V_r and Γ, are listed in the third column in Table 2. The SMGA is 118.6 km^2 (10.89 × 10.89 km), the stress drop is 12.9 MPa, and the seismic moment of SMGA is 6.85×10^{18} N·m. The location of the SMGA, as shown in Fig. 3, nearly coincides with the large slip area of the inverted kinematic source model (Li et al. 2017), which suggests that the SMGA can be regarded as equivalent to an asperity. Figure 4 shows the comparisons of waveforms between synthesized and observed acceleration, velocity and displacement in the NS and EW components at seven target stations. Figure 5 shows the comparisons of the acceleration Fourier spectra between synthesized and observed ground motions.
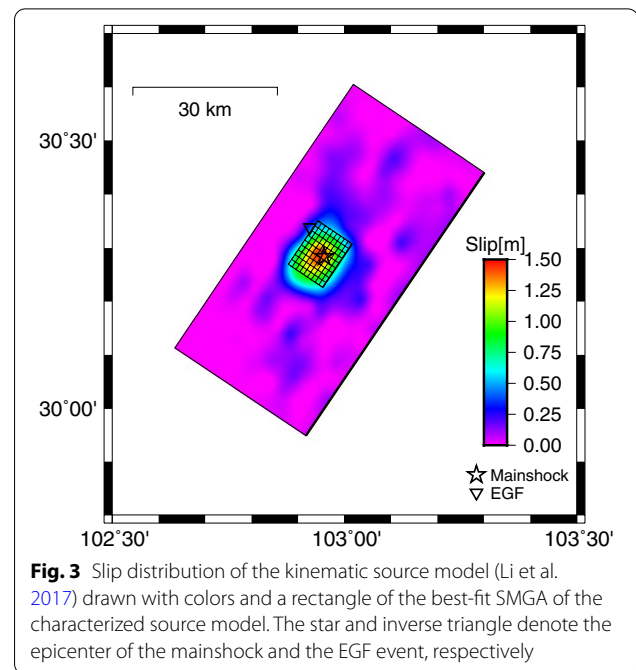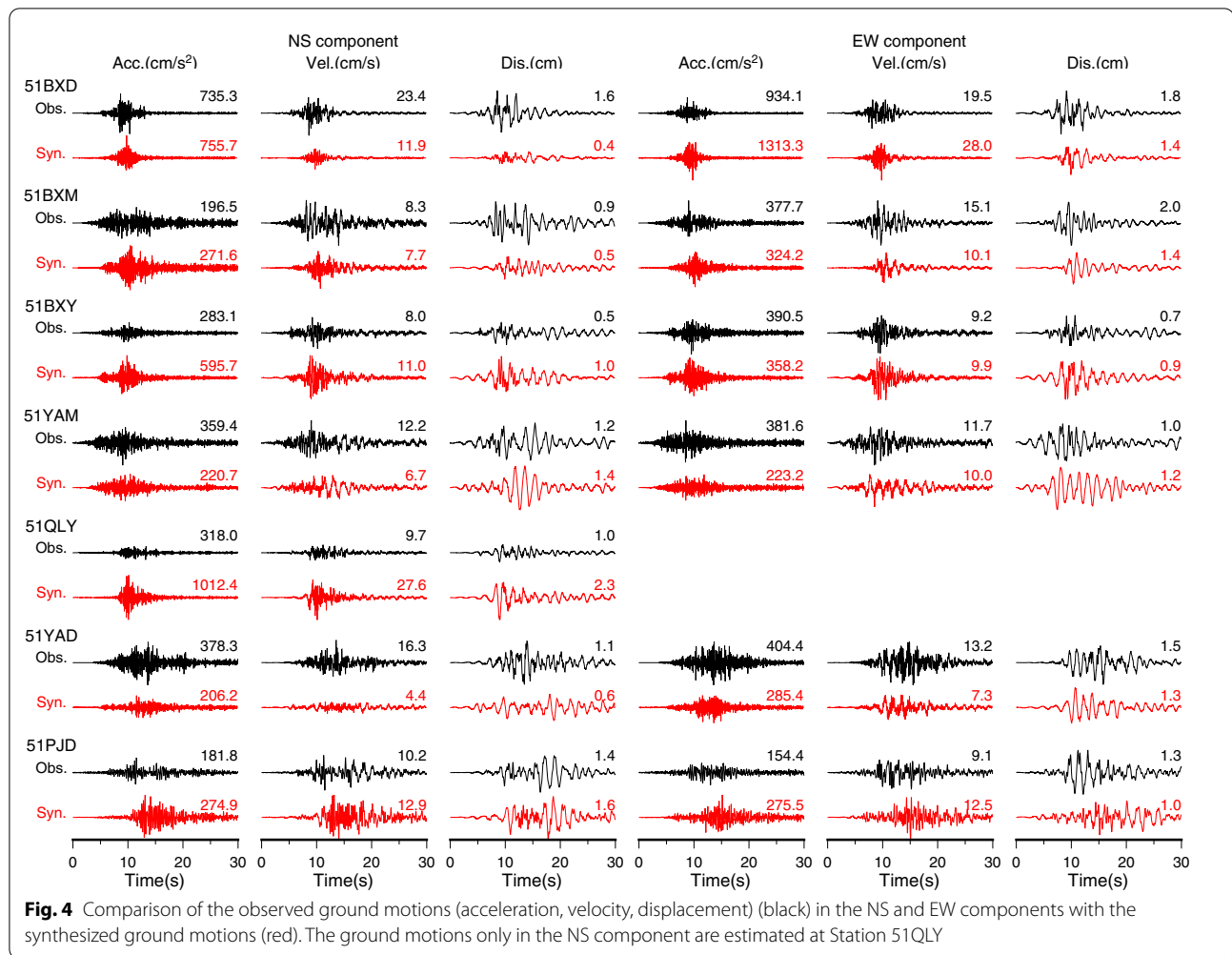

Fig. 3 Slip distribution of the kinematic source model (Li et al. 2017) drawn with colors and a rectangle of the best-fit SMGA of the characterized source model. The star and inverse triangle denote the epicenter of the mainshock and the EGF event, respectively
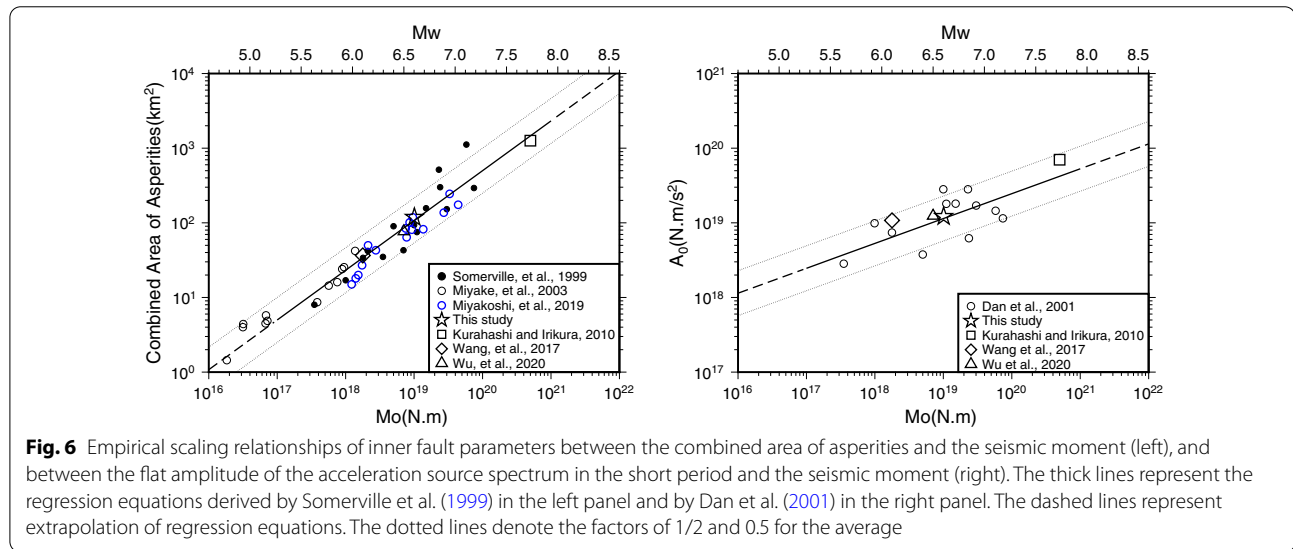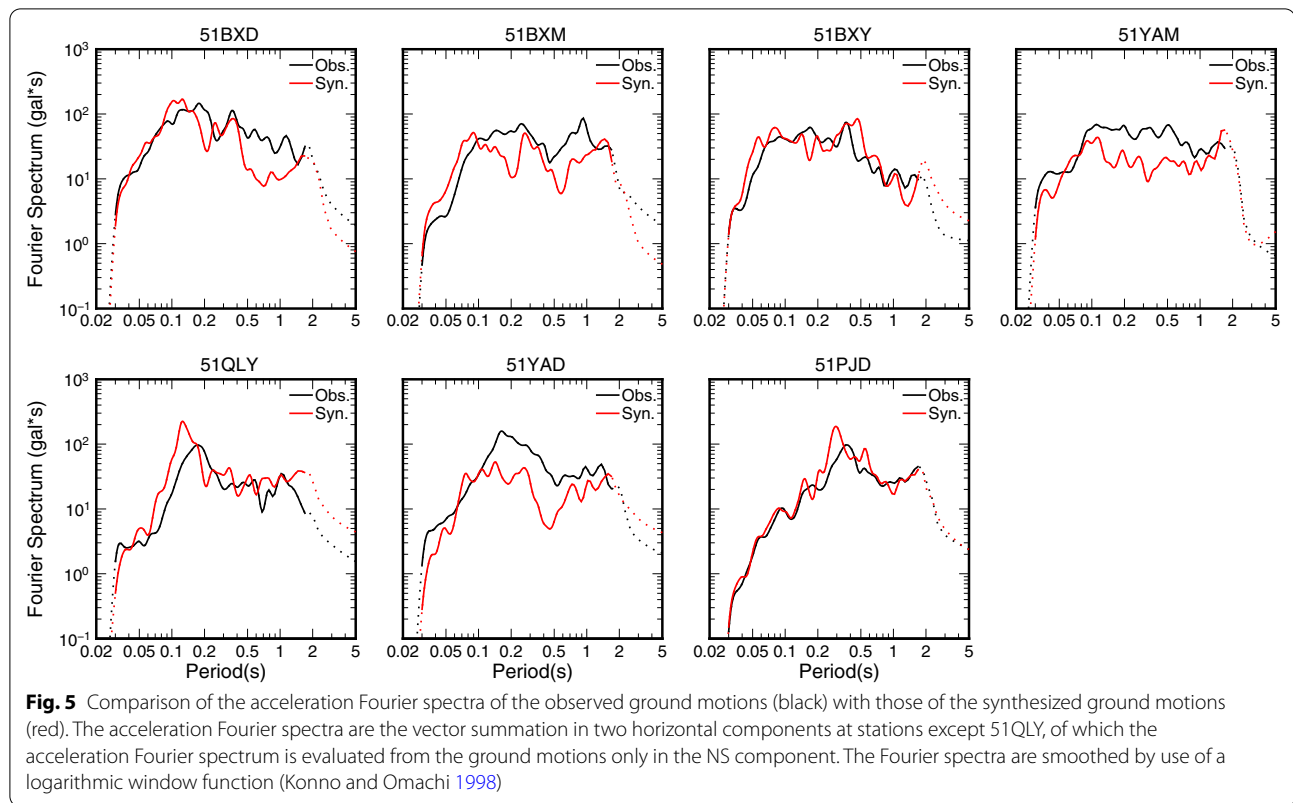
The Fourier spectra are smoothed using a logarithmic window function with a band width parameter of b = 50 (Konno and Omachi 1998). Overall, not only the waveforms but also the Fourier spectra of the synthesized ground motions are in fairly good agreement with the counterparts of the observed ground motions at the target stations except for some stations, where synthesized acceleration waveforms are overestimated as nonlinearity of surface geology is not included in the EGFM. We also applied the same set of parameters of the best-fit SMGA to synthesize the ground motions at three non-target stations, i.e., 51PJW, 51DJZ, and 51CDZ, where the observed ground motions are not considered in the above inversion analysis. The good consistency between the synthesized and observed ground motions is confirmed (Additional file 1: Fig. S1 and Additional file 2: Fig. S2), which further suggests that the characterized source model consisting of one SMGA is suitable for synthesizing the ground motions of the mainshock.

Subsequently, we examined the effectiveness of the inner fault parameters, such as the SMGA and acceleration level, in the best-fit source model. Here, the SMGA is considered equivalent to the combined area of an asperity. Figure 6 shows the empirical scaling relationship between the combined area of asperities with large slips estimated from waveform inversions for long-period (> 1.0 s) motion and the seismic moment (M_o) proposed by Somerville et al. (1999) and Irikura and Miyake (2001, 2011) in the left panel, and the empirical scaling relationship between the flat amplitude of the acceleration source

Wu *et al. Earth, Planets and Space*   (2022) 74:50

Page 8 of 15

Fig. 4 Comparison of the observed ground motions (acceleration, velocity, displacement) (black) in the NS and EW components with the synthesized ground motions (red). The ground motions only in the NS component are estimated at Station 51QLY

spectrum in the short period (A_0) (estimated according to Eq. (15), Dan et al. 2001) and M_o proposed by Dan et al. (2001) in the right panel. The relationship between the SMGA and M_o and the relationship between the A_0 and M_o of the best-fit characterized source model during the 2013 Lushan earthquake (M_w 6.6) are found to be similar to these two empirical scaling relationships. Furthermore, we added the results of the SMGAs of the 2008 Wenchuan earthquake (M_w 7.9) (Kurahashi and Irikura 2010) and those of the 2014 Ludian earthquake (M_w 6.1) (Wang et al. 2017) and the 2017 Jiuzhaigou earthquake (M_w 6.5) (Wu et al. 2020), as shown with square, diamond and solid circle, respectively, in Fig. 6. It should be noted that Kurahashi and Irikura (2010) constructed the characterized source model only in the southern part of the fault model, and the seismic moment in the southern part was assumed to be half of the seismic moment for the entire fault. The relationships between the SMGAs
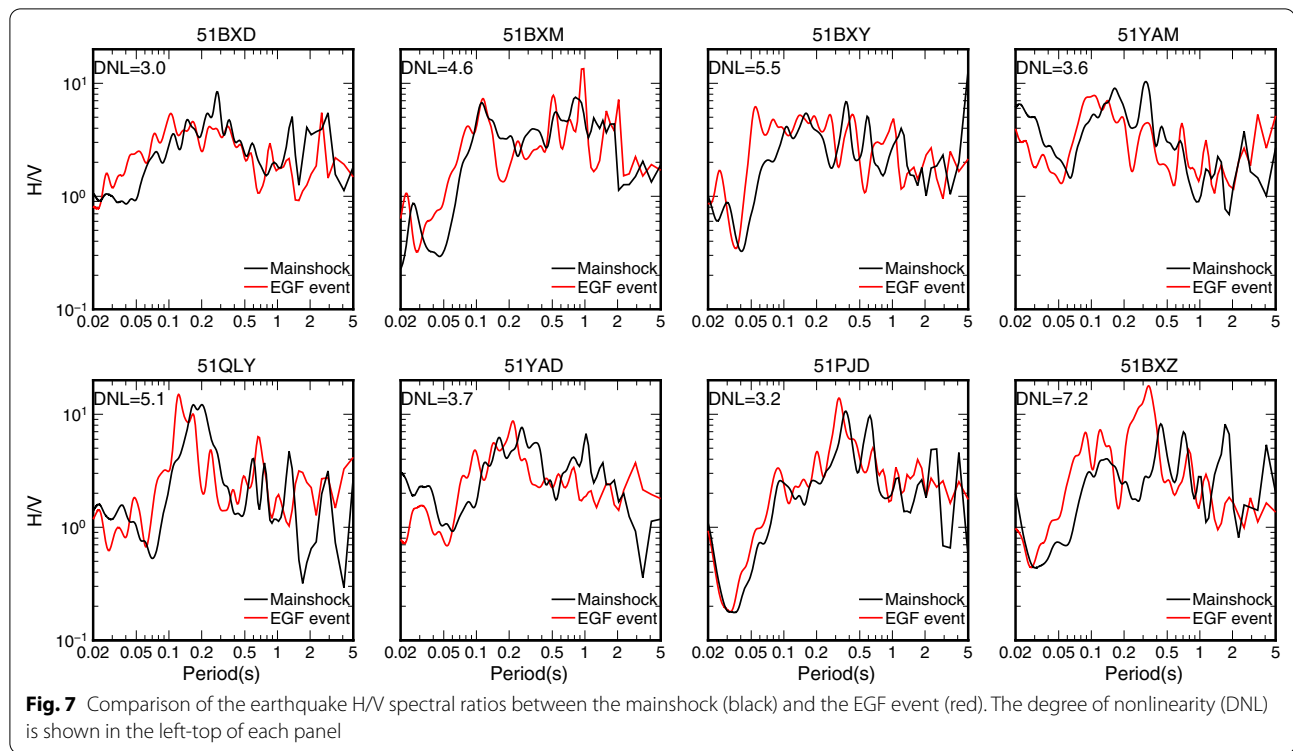
and M_o for these crustal earthquakes in China agree well with the empirical scaling relationship (Somerville et al. 1999; Irikura and Miyake 2001, 2011; Miyake et al. 2003; Miyakoshi et al. 2020). The A_0 values for the 2014 Ludian earthquake and the 2008 Wenchuan earthquake are slightly larger than those estimated from the empirical scaling relation, which is acceptable, as the values fall in the range indicating factors of 1/2 and 2 for the average (shown in dotted lines). Therefore, the relationships between A_0 and M_o for these crustal earthquakes also follow an empirical scaling relationship (Dan et al. 2001). This implies that the empirical scaling relationships of inner fault parameters might be applicable to estimate the inner fault parameters for future crustal earthquakes in China. More inner fault parameters of the characterized source models for crustal earthquakes in China (if any) are required to investigate the applicability of the empirical scaling relationships.

Wu *et al. Earth, Planets and Space* (2022) 74:50

Page 9 of 15

Fig. 5 Comparison of the acceleration Fourier spectra of the observed ground motions (black) with those of the synthesized ground motions (red). The acceleration Fourier spectra are the vector summation in two horizontal components at stations except 51QLY, of which the acceleration Fourier spectrum is evaluated from the ground motions only in the NS component. The Fourier spectra are smoothed by use of a logarithmic window function (Konno and Omachi 1998)

Fig. 6 Empirical scaling relationships of inner fault parameters between the combined area of asperities and the seismic moment (left), and between the flat amplitude of the acceleration source spectrum in the short period and the seismic moment (right). The thick lines represent the regression equations derived by Somerville et al. (1999) in the left panel and by Dan et al. (2001) in the right panel. The dashed lines represent extrapolation of regression equations. The dotted lines denote the factors of 1/2 and 0.5 for the average
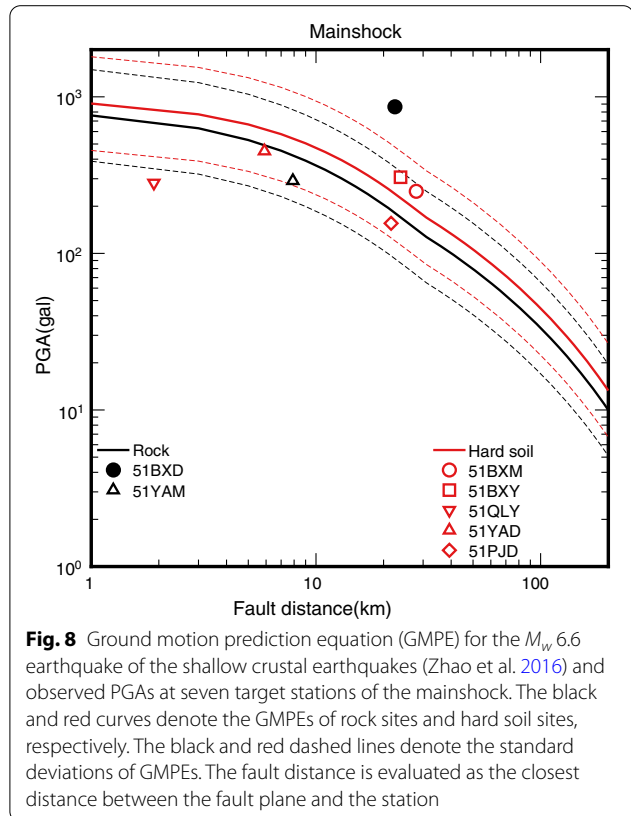
Discussion

The EGFM is applicable for synthesizing the ground motions on the premise of linear superposition of the EGF, while the nonlinear effects on the ground motions are excluded for applying the EGFM. To examine the influence of nonlinearity on the surface geology of observed ground motions, we compare the earthquake H/V spectral ratio of the mainshock with that of the
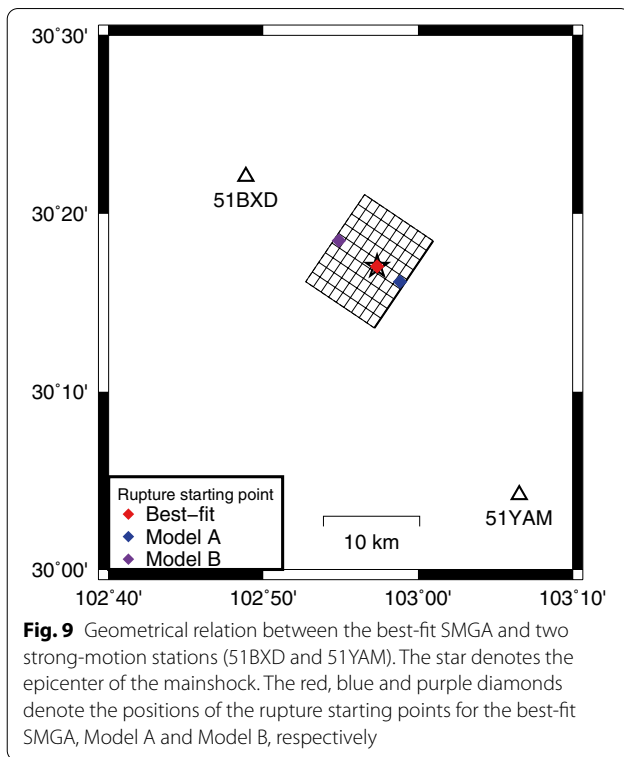
EGF event at seven target stations in Fig. 7. The acceleration Fourier spectra in three components are calculated from the S-wave portions with a time length of 20.48 s, and then the H/V spectral ratios are evaluated following the method of Kawase et al. (2011). The degree of nonlinearity (DNL) (Noguchi and Sasatani 2008) at each station is evaluated to represent the extent of the nonlinear effect. A large DNL suggests a strong nonlinear

Fig. 7 Comparison of the earthquake H/V spectral ratios between the mainshock (black) and the EGF event (red). The degree of nonlinearity (DNL) is shown in the left-top of each panel

effect, and vice versa. The similarity of the earthquake H/V spectral ratios between the mainshock and the EGF event and the small values of DNLs indicate that nonlinear effects are sufficiently weak at some target stations. Although the observed PGA of the mainshock is quite large at Station 51BXD, the smallest DNL value suggests that the nonlinear behavior of the site is negligible there. This is consistent with the fact that the site condition is rock, and the field survey also reported that the station was situated on the slope of a small rock hill (Wen and Ren 2014). The moderate values of DNL at Stations 51BXY and 51QLY suggest that the nonlinear behaviors of the sites are moderate. The synthesized acceleration ground motions are slightly larger than the observed ground motions at these stations due to the linear premise of the EGFM. An exception is the 51BXZ station, where the largest value of DNL suggests that nonlinear behavior is quite strong, which should be excluded when synthesizing the ground motions of the mainshock. The synthesis through the EGFM taking the nonlinear effect into account could be accomplished by introducing certain parameters (Nozu and Morikawa 2003), which is beyond the scope of this study.
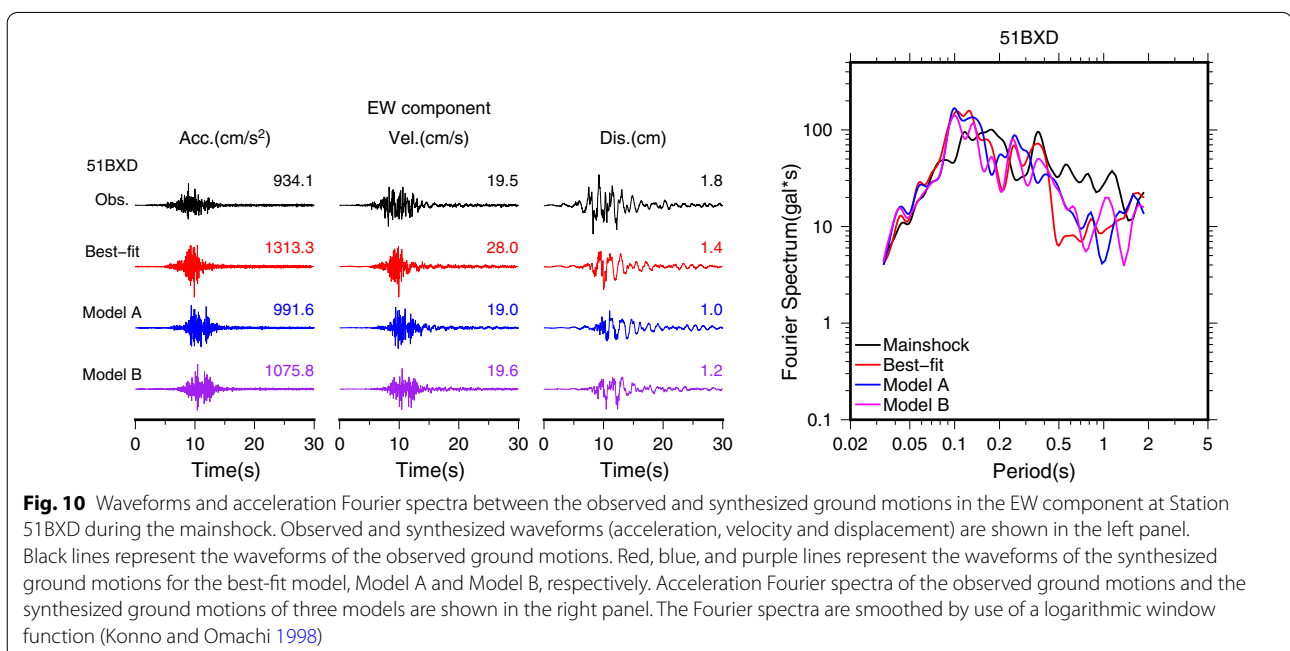
Figure 8 compares the observed PGAs at target stations with those predicted by the ground motion prediction equations (GMPEs) (Zhao et al. 2016). The site conditions of the target stations can be categorized
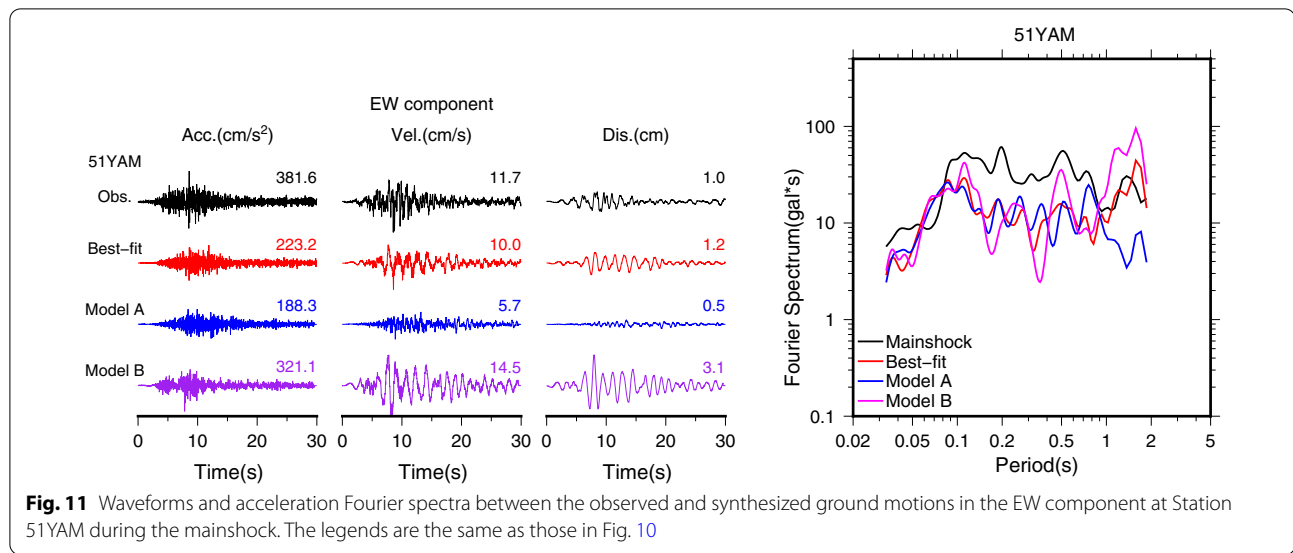

Fig. 8 Ground motion prediction equation (GMPE) for the M_w 6.6 earthquake of the shallow crustal earthquakes (Zhao et al. 2016) and observed PGAs at seven target stations of the mainshock. The black and red curves denote the GMPEs of rock sites and hard soil sites, respectively. The black and red dashed lines denote the standard deviations of GMPEs. The fault distance is evaluated as the closest distance between the fault plane and the station

Fig. 9 Geometrical relation between the best-fit SMGA and two strong-motion stations (51BXD and 51YAM). The star denotes the epicenter of the mainshock. The red, blue and purple diamonds denote the positions of the rupture starting points for the best-fit SMGA, Model A and Model B, respectively
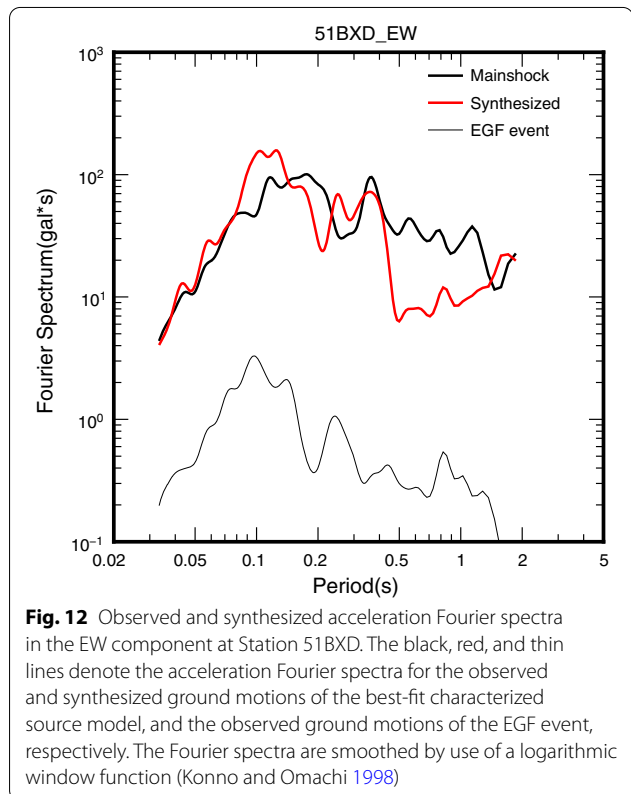
the black curves to show GMPEs for the rock site and the red curves for the hard soil site. The observed PGAs are comparable with the predicted PGAs within one standard deviation at target stations except the 51BXD station, where the observed PGA is abnormally larger than the predicted PGA. The source effect (e.g., directivity effect), site effect (e.g., nonlinear behavior, large shear-wave velocity contrast, topographic effect) and hanging-wall effect could be considered the reasons. We investigated the directivity effect on the ground motions in the EW component at the 51BXD and 51YAM stations by comparing the synthesized ground motions for different rupture-starting points: hypocenter (best-fit SMGA), top of the SMGA (Model A), and bottom of the SMGA (Model B), as illustrated in Fig. 9. Figures 10 and 11 show the results of waveforms and acceleration Fourier spectra in the EW component for the above three models, as well as the observed results during the mainshock, at Stations 51BXD and 51YAM. The amplitude of the acceleration Fourier spectrum of the synthesized ground motion at Station 51BXD for Model A is similar to that for Model B at periods below 0.3 s. This suggests that the directivity has little effect on the short-period ground motions. On the other hand, the amplitude of the acceleration Fourier spectrum of the synthesized ground motion at Station 51BXD for Model A is larger than that for Model B at periods of $1.0 \sim 2.0$ s. This indicates that the directivity affects the long-period ground motions at Station 51BXD, which is in the

into two classes, i.e., rock and hard soil, according to the average shear-wave velocity within 30 m in depth (Vs30) (Xie et al. 2022), the predominant period of the H/V response spectral ratio or field survey, we employ

Fig. 10 Waveforms and acceleration Fourier spectra between the observed and synthesized ground motions in the EW component at Station 51BXD during the mainshock. Observed and synthesized waveforms (acceleration, velocity and displacement) are shown in the left panel. Black lines represent the waveforms of the observed ground motions. Red, blue, and purple lines represent the waveforms of the synthesized ground motions for the best-fit model, Model A and Model B, respectively. Acceleration Fourier spectra of the observed ground motions and the synthesized ground motions of three models are shown in the right panel. The Fourier spectra are smoothed by use of a logarithmic window function (Konno and Omachi 1998)

Fig. 11 Waveforms and acceleration Fourier spectra between the observed and synthesized ground motions in the EW component at Station 51YAM during the mainshock. The legends are the same as those in Fig. 10

forward direction of rupture propagation (Model A). Moreover, the synthesized waveforms of Model A are in better agreement with the observed waveforms than those of the best-fit characterized source model. However, if we compare the synthesized ground motions with the observed ones at other stations, e.g., 51YAM, as shown in Fig. 11, the synthesized ground motions of Model A are in poorer agreement with the observed ones than those of the best-fit SMGA model. In terms of the fitting of the synthesized ground motions at all target stations, the best-fit SMGA source model is preferred among the three models. Furthermore, the amplitude of the acceleration Fourier spectrum of Model B is quite larger at periods of 1.0 ~ 2.0 s than that of the other two models at Station 51YAM. This indicates that the directivity effect is noticeable at Station 51YAM, which is in the forward direction of rupture propagation (Model B). In contrast, the directivity effect is not significant at Station 51BXD even though the station is in the forward direction of rupture propagation (Model A). This is because the SMGA dips toward the northwest and the distances between each subfault of the SMGA and the 51BXD station are not as variant when the rupture propagates toward the 51BXD station. We concluded that the directivity effect could not be responsible for the largest PGA in the EW component at Station 51BXD station for the best-fit SMGA source model of which the rupture starting point is close to the center of the SMGA.

In addition, the synthesized ground motions for the best-fit SMGA of the characterized source model agree with the observed ground motions in the EW component at Station 51BXD during the mainshock, as shown in Fig. 4 and Fig. 5. The largest PGA can be attributed to

Fig. 12 Observed and synthesized acceleration Fourier spectra in the EW component at Station 51BXD. The black, red, and thin lines denote the acceleration Fourier spectra for the observed and synthesized ground motions of the best-fit characterized source model, and the observed ground motions of the EGF event, respectively. The Fourier spectra are smoothed by use of a logarithmic window function (Konno and Omachi 1998)

the large peak of the Fourier spectrum at approximately 0.1 s which was observed during the mainshock and the EGF event, as shown in Fig. 12. On the other hand, if strong site amplification contributes to the largest record, it must be caused by the large shear-wave velocity contrast between the soft and hard soils in the shallow layers. However, soft soil might not exist, as the station is

situated on the slope of a small rock hill. It is appropriate to attribute the reason to the hanging-wall effect and topographic effect which have been investigated in the previous studies (Dai and Li 2013; Xie et al. 2014; Wen and Ren 2014).

Conclusions

We successfully reproduced the ground motions for the mainshock during the 2013 Lushan earthquake (M_w 6.6) using the characterized source model and the empirical Green's function method (EGFM). The source parameters of the best-fit source model are determined by applying the adaptive simulated annealing (ASA) algorithm (Satoh 2006) for the misfit function by Miyake et al. (1999) using the waveforms in a frequency range from 0.5 to 30.0 Hz at seven near-source strong motion stations. The best-fit characterized source model consists of one strong motion generation area (SMGA) and a background area. We also confirmed the good consistency between the synthesized and observed ground motions at the other three strong-motion stations, where the observed ground motions were not used for the inversion analysis when the same set of parameters was employed to synthesize the ground motions there.

We found the relationships between the SMGA and M_o and the relationships between the flat amplitude of the acceleration source spectrum in the short period and M_o, for the characterized source model of the 2013 Lushan earthquake (M_w 6.6), together with the 2014 Ludian earthquake (M_w 6.1), the 2017 Jiuzhaigou earthquake (M_w 6.5) and the 2008 Wenchuan earthquake (M_w 7.9), followed the empirical scaling relationships of inner fault parameters (e.g., Somerville et al. 1999; Irikura and Miyake 2001, 2011; Dan et al. 2001). This implied that the empirical scaling relationships of inner fault parameters might be applicable for the prediction of strong ground motions for future crustal earthquakes in China.

The largest PGA during this earthquake was larger than 1 g at Station 51BXD, where large strong motions exceeding 1 g were obtained for the first time in the observation history of China. We explored the reason for the largest record from the source effect (e.g., directivity effect) and site effect (e.g., nonlinear behavior, large shear-velocity contrast, topographic effect). Our analyses suggested that the directivity effect cannot be the reason for comparing the effect of different positions of the rupture-starting point on the synthesized ground motions and that the nonlinear effect was not strong, as indicated by the similarity of the earthquake H/V spectral ratios between the mainshock and the EGF event. The Fourier spectra of the observed ground motions of both the mainshock and the EGF event dominated in the same short-period range (e.g., 0.1 ~ 0.2 s), which was responsible for the largest

PGA. This result suggested that the strong site amplification, if present, was caused by the large shear-wave velocity contrast between the soft and hard soils in the shallow layers. However, we considered this impossible, as the station was situated on the slope of a small rock hill. Finally, we agreed with the previous studies (Dai and Li 2013; Xie et al. 2014; Wen and Ren 2014) that the hanging-wall effect and topographic effect could be the reasons for generating the largest record at Station 51BXD.

Abbreviations
ASA: Adaptive simulated annealing; EGF: Empirical Green's function; EGFM: Empirical Green's function method; DNL: Degree of nonlinearity; PGA: Peak ground acceleration; SMGA: Strong motion generation area; Vs30: Average shear-wave velocity within 30 m in depth.

Supplementary Information
The online version contains supplementary material available at https://doi.org/10.1186/s40623-022-01613-6.

Additional file 1: Figure S1. Comparison of the observed ground motions (acceleration, velocity, displacement) (black) in the NS and EW components with the synthesized ground motions (red) at the 51PJW, 51DJZ and 51CDZ stations.

Additional file 2: Figure S2. Comparison of the acceleration Fourier spectra (black) of the observed ground motions with those of the synthesized ground motions (red) at the 51PJW, 51DJZ and 51CDZ stations. The Fourier spectra are smoothed by use of a logarithmic window function (Konno and Omachi 1998).

Author contributions
HW designed the study, analyzed the data and drafted the manuscript. KI designed the study, participated in discussions, and interpreted the results. KM and KS contributed to discussions of the data processing and the results. All authors read and approved the final manuscript.

Availability of data and materials
The data sets analyzed during the current study are available from the corresponding author on reasonable request.

Declarations

Ethics approval and consent to participate
Not applicable.

Consent for publication
Not applicable.

Wu *et al. Earth, Planets and Space*   (2022) 74:50

Page 14 of 15

Author details
[1] School of Civil Engineering, Shandong Jianzhu University, Fengming Road 1000, Jinan, Shandong 250101, China. [2] Disaster Prevention Research Center, Aichi Institute of Technology, Yachigusa 1247, Yakusa-cho, Toyota 470-0392, Japan. [3] Geo-Research Institute, Otemae 2-1-2, Chuo-ku, Osaka 540-0008, Japan.

References
Boatwright J (1988) The seismic radiation from composite models of faulting. Bull Seismol Soc Am 78:489–508. https://doi.org/10.1785/BSSA0780020489

Brune JN (1970) Tectonic stress and spectra of seismic shear waves from earthquakes. J Geophys Res 75:4997–5009. https://doi.org/10.1029/JB075i026p04997

Brune JN (1971) Correction. J Geophys Res 76(20):5002. https://doi.org/10.1029/JB076i020p05002

Dai ZJ, Li XJ (2013) An explanation of the large PGA value of the 2013 Ms 7.0 Lushan earthquake at 51BXD station through topographic analysis. Earthq Sci 26(3–4):199–205. https://doi.org/10.1007/s11589-013-0043-y

Dan K, Watanabe M, Sato T, Ishi T (2001) Short-period source spectra inferred from variable-slip rupture models and modeling of earthquake faults for strong motion prediction by semi-empirical method. J Struct Const Eng 545:51–62 (**in Japanese with English abstract**)

Deng QD, Zhang P, Ran Y, Yang X, Min W, Chu Q (2003) Basic characteristics of active tectonics of China. Sci Chin 46(4):356–372

Eshelby JD (1957) The determination of the elastic field of an ellipsoidal inclusion and related problems. Proc R Soc London Ser A 241:376–396. https://doi.org/10.1098/rspa.1957.0133

Han LB, Zeng XF, Jiang CS, Ni SD, Zhang HJ, Long F (2014) Focal mechanisms of the 2013 Mw 6.6 Lushan, China earthquake and high-resolution aftershock relocations. Seismol Res Lett 85(1):8–14. https://doi.org/10.1785/0220130083

Hao JL, Ji C, Wang WM, Yao ZX (2013) Rupture history of the 2013 M_w 6.6 Lushan earthquake constrained with local strong motion and teleseismic body and surface waves. Geophys Res Lett 40:5371–5376. https://doi.org/10.1002/2013GL056876

Hartzell SH (1978) Earthquake aftershocks as Green's functions. Geophys Res Lett 5:1–4. https://doi.org/10.1029/GL005i001p00001

Irikura K (1983) Semi-empirical estimation of strong ground motions during large earthquakes. Bull Disaster Prev Res Inst Kyoto Univ 33:63–104

Irikura K, Miyake H (2001) Prediction of strong ground motions for scenario earthquakes. J Geogr 110(6):849–875 (**in Japanese with English abstract**)

Irikura K, Miyake H (2011) Recipe for predicting strong ground motion from crustal earthquake scenarios. Pure Appl Geophys 168:85–104. https://doi.org/10.1007/s00024-010-0150-9

Irikura K, Kagawa T, Sekiguchi H (1997) Revision of the empirical Green's function method by Irikura (1986). Programme and abstracts of the Seismological Society of Japan, 2 (in Japanese)

Irikura K (1986) Prediction of strong acceleration motions using empirical Green's function. In: Proc 7th Japan earthquake engineering symposium, Tokyo: 151–156

Kamae K, Irikura K (1992) Prediction of site-specific strong ground motion using semi-empirical methods. In: Proc 10th World Conference on Earthquake Engineering, Madrid, Spain. p 801–806

Kamae K, Irikura K (1998) Source model of the 1995 Hyogo-ken Nanbu earthquake and simulation of near-source ground motion. Bull Seismol Soc Am 88(2):400–412. https://doi.org/10.1785/BSSA0880020400

Kanamori H (1979) A semi-empirical approach to prediction of long-period ground motions from great earthquakes. Bull Seismol Soc Am 69:1645–1670. https://doi.org/10.1785/BSSA06900616451

Kawase H, Sánchez-Sesma FJ, Matsushima S (2011) The optimal use of horizontal-to-vertical spectral ratios of earthquake motions for velocity inversion based on diffuse-field theory for plane waves. Bull Seismol Soc Am 101(5):2001–2014. https://doi.org/10.1785/0120100263

Konno K, Omachi T (1998) Ground-motion characteristics estimated from spectral ratio between horizontal and vertical components of microtremor. Bull Seismol Soc Am 88:228–241. https://doi.org/10.1785/BSSA0880010228

Kurahashi S, Irikura K (2010) Characterized source model for simulating strong ground motions during the 2008 Wenchuan earthquake. Bull Seismol Soc Am 100(5B):2450–2475. https://doi.org/10.1785/0120090308

Kurahashi S, Irikura K (2013) Short-period source model of the 2011 Mw 9.0 off the Pacific coast of Tohoku earthquake. Bull Seismol Soc Am 103(2B):1373–1393. https://doi.org/10.1785/0120120157

Li J, Liu CL, Zheng Y, Xiong X (2017) Rupture process of the Ms 7.0 Lushan earthquake determined by joint inversion of local static GPS records, strong motion data, and teleseismograms. J Earth Sci 28(2):404–410. https://doi.org/10.1007/s12583-017-0757-1

Liu CL, Zheng Y, Ge C, Xiong X (2013) Hsu HT (2013) Rupture process of the Ms 7.0 Lushan earthquake. Sci Chin Earth Sci 56(7):1187–1192. https://doi.org/10.1007/s11430-013-4639-9

Miyake H, Iwata T, Irikura K (1999) Strong ground motion simulation and source modeling of the Kagoshima-ken Hokuseibu earthquakes of March 26 (M_{JMA} 6.5) and May 13 (M_{JMA} 6.3), 1997, using empirical Green's function method. Zisin 51:431–442 (**in Japanese with English abstract**)

Miyake H, Iwata T, Irikura K (2003) Source characterization for broadband ground-motion simulation: kinematic heterogeneous source model and strong motion generation area. Bull Seismol Soc Am 93(6):2531–2545. https://doi.org/10.1785/0120020183

Miyakoshi K, Somei K, Yoshida K, Kurahashi S, Irikura K, Kamae K (2020) Scaling relationships of source parameters of inland crustal earthquakes in tectonically active regions. Pure Appl Geophys 177:1917–1929. https://doi.org/10.1007/s00024-019-02160-0

Noguchi S, Sasatani T (2008) Quantification of degree of nonlinear site response. In: Proc 14th World Conference on Earthquake Engineering, Beijing, China

Nozu A, Morikawa H (2003) An empirical Green's function method considering multiple nonlinear effects. Zisin 2(55):361–374 (**in Japanese with English abstract**)

Nozu A (2006) A simple scheme to introduce near-field and intermediate-field terms in stochastic Green's functions. In: Proc 12th Japan Earthquake Engineering Symposium. p 190–193 (in Japanese with English abstract)

Satoh T (2006) Inversion of Qs of deep sediments from surface-to-borehole spectral ratios considering obliquely incident SH and SV waves. Bull Seismol Soc Am 96(3):943–956. https://doi.org/10.1785/0120040179

Somei K, Miyakoshi K, Yoshida K, Kurahashi S, Irikura K (2020) Near-source strong pulses during two large Mjma 6.5 and Mjma 7.3 events in the 2016 Kumamoto, Japan, earthquakes. Pure Appl Geophys 177:2223–2240. https://doi.org/10.1007/s00024-019-02095-6

Somerville P, Irikura K, Graves R, Sawada S, Wald D, Abrahamson N, Iwasaki Y, Kagawa T, Smith N, Kowada A (1999) Characterizing crustal earthquake slip models for the prediction of strong ground motion. Seismol Res Lett 70(1):59–80. https://doi.org/10.1785/gssrl.70.1.59

Tao ZR, Tao XX, Cui AP (2016) Strong motion PGA prediction for southwestern China from small earthquake records. Nat Hazards Earth Syst Sci 16:1145–1155. https://doi.org/10.5194/nhess-16-1145-2016

Wang X, Kurahashi S, Wu H, Si HJ, Ma Q, Dang J, Tao DW, Feng JW, Irikura K (2017) Building damage concentrated in Longtoushan town during the 2014 Ms 6.5 Ludian earthquake, Yunan, China: examination of cause and implications based on ground motion and vulnerability analyses. J Seismol 21(5):1185–1200. https://doi.org/10.1007/s10950-017-9659-z

Wen RZ, Ren YF (2014) Strong-motion observations of the Lushan earthquake on 20 April 2013. Seismol Res Lett 85(5):1043–1055. https://doi.org/10.1785/0220140006

Wessel P, Smith WHF, Scharroo R, Luis J, Wobbe F (2013) Generic mapping tools: improved version released. EOS Trans AGU 94(45):409–410. https://doi.org/10.1002/2013EO450001

Wu H, Irikura K, Kurahashi S (2020) Characterized Source Model of the 2017 M_w 6.5 Jiuzhaigou Earthquake. In: Proc 17th World Conference on Earthquake Engineering, No. 1b-0004, Sendai, Japan

Xie JJ, Li XJ, Wen ZP, Wu CQ (2014) Near-source vertical and horizontal strong ground motion from the 20 April 2013 Mw 6.8 Lushan Earthquake in China. Seismol Res Lett 85(1):23–33. https://doi.org/10.1785/0220130121

Wu *et al. Earth, Planets and Space*   (2022) 74:50

Page 15 of 15

Xie JJ, Li XJ, Wen ZP, Jia L, An Z, Cui JW, Lin GL, Zhang Q, Jiang P, Xie QC, Wang PF, Zimmaro P, Stewart JP (2022) Soil profile database and site classification for national strong-motion stations in western China. Seismol Res Lett. https://doi.org/10.1785/0220210271

Yi GX, Long F, Amaury V, Klinger Y, Liang MJ, Wang SW (2016) Focal mechanism and tectonic deformation in the seismogenic area of the 2013 Lushan earthquake sequence, southwestern China. Chin J Geophys 59(10):3711–3731. https://doi.org/10.6038/cjg20161017 (**in Chinese with English abstract**)

Zhang Y, Wang RJ, Chen YT, Xu LS, Du F, Jin MP, Tu HW, Dahm T (2014) Kinematic rupture model and hypocenter relocation of the 2013 Mw 6.6 Lushan earthquake constrained by strong-motion and teleseismic data. Seismol Res Lett 85(1):15–22. https://doi.org/10.1785/0220130126

Zhao JX, Zhou SL, Zhou J, Zhao C, Zhang H, Zhang YB, Gao PJ, Lan XW, Rhoades D, Fukushima Y, Somerville PG, Irikura K (2016) Ground-motion prediction equations for shallow crustal and upper-Mantle earthquakes in Japan using site class and simple geometric attenuation in functions. Bull Seismol Soc Am 106(4):1552–1569. https://doi.org/10.1785/0120150063

Publisher's Note

Springer Nature remains neutral with regard to jurisdictional claims in published maps and institutional affiliations.